CHEMISTRY OF MATERIALS
Cite This: Chem. Mater. 2019, 31, 10017−10022
Article
pubs.acs.org/cm

Three-Dimensional Printing of Hierarchical Porous Architectures

Jen-Yu Huang,[†] Hong Xu,[‡] Eliad Peretz,[§,∥] Dung-Yi Wu,[‡] Christopher K. Ober,[‡] and Tobias Hanrath*[,†]

[†]Robert F. Smith School of Chemical and Biomolecular Engineering, [‡]Department of Materials Science and Engineering, and [§]Sibley School of Mechanical and Aerospace Engineering, Cornell University, Ithaca, New York 14853, United States
[∥]NASA Goddard Spaceflight Center, Greenbelt, Maryland 20771, United States

Supporting Information

ABSTRACT: Concurrent advances in the programmable synthesis of nanostructured materials and additive three-dimensional (3D) manufacturing have created a rich and exciting opportunity space to fabricate novel materials and devices. In particular, creating complex hierarchical device geometries from mesoporous materials presents several scientifically interesting and technologically relevant challenges. Here, we show how digital light processing of photoresponsive building block defined by an oxozirconium methacrylate cluster with 12 methacrylic acid ligands can be used to enable the creation of complex superstructures characterized by multilevel porous networks. Inspired by similarly complex 3D hierarchical mesoporous structures ubiquitous in nature, we demonstrated the fabrication of a 3D leaf as a proof of concept. This work demonstrates how exciting opportunity space emerging at the intersection of inorganic building blocks, mesoporous materials, and 3D digital light processing opens new pathways to create functional hierarchical superstructures and devices with complex geometries.

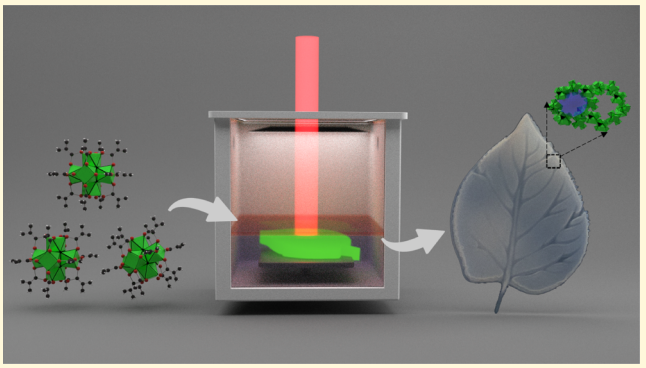

Nature is replete with hierarchical structures designed with the macroscopic shape and nanoscale details. Natural systems are formed via a beautifully orchestrated bottom-up assembly strategy spanning multiple length scales from amino acids, protein chains, cells, tissues, to organs.[1] The ability of natural systems to spontaneously self-assemble into complex, hierarchical, multifunctional structures provides an intriguing inspiration to create biomimetic hierarchical structures.[1,2] Analogous hierarchical assembly strategies in synthetic systems (e.g., metal−organic frameworks)[3] have intrigued scientists and engineers for years. However, whereas the diversity of the library of available nanostructured building blocks continues to grow, our ability to fabricate porous three-dimensional (3D) structures with programmable geometries from these building blocks is still in its infancy compared to the complexity commonly found in natural systems.[4] Successful formation of hierarchical porous structures that integrate features and functions spanning nano-, meso-, and macroscales[5,6] has significant implications for a broad range of applications.[7−10]

Among the various nonbiological bottom-up fabrication methods, additive manufacturing, also well known as 3D printing, has emerged as an attractive option to fabricate sophisticated 3D geometries at macroscopic length scales.[11−13] Digital light processing (DLP) 3D printing is a photoresin-based additive manufacturing technique, which has come into focus by virtue of the rapid speed (50 cm/h), micrometer resolution, and low-cost desktop-level system, increasing the accessibility at large.[14,15] The general workflow for this fabrication method is to create 3D objects by digitally slicing the desired 3D architecture into a series of images, which are then exposed as a sequence of ultraviolet (UV) patterns to define the cross section for each additive layer (Figure 1A).

Attaching a photoresponsive ligand to the surface of an inorganic core opens a broad opportunity space to leverage recent concurrent advances in digital light processing and colloidal nanoscale materials. To provide a proof of concept of the photoresponsive ligand on inorganic core (PLIC) chemistry, we functionalized the surface of oxozirconium clusters with methacrylate groups. Our choice of oxozirconium clusters was inspired, in part, by the fact that porous inorganic materials synthesized by solvothermal methods are very challenging to processing into complex geometries due to their brittle mechanical properties.[4] To overcome this limitation, the PLIC fabrication scheme introduced here uses light to spatially program where the building blocks are connected and form nanoscale porosity in situ. The inorganic core and organic ligand combined on the molecular scale generate a synergetic combination of innate properties from each component. Using PLIC as 3D printing inks, we can manipulate predesigned structures in different length scales by combining the inherent porosity of connecting PLIC units at

Received: July 11, 2019
Revised: September 28, 2019
Published: October 7, 2019

DOI: 10.1021/acs.chemmater.9b02761
Chem. Mater. 2019, 31, 10017−10022

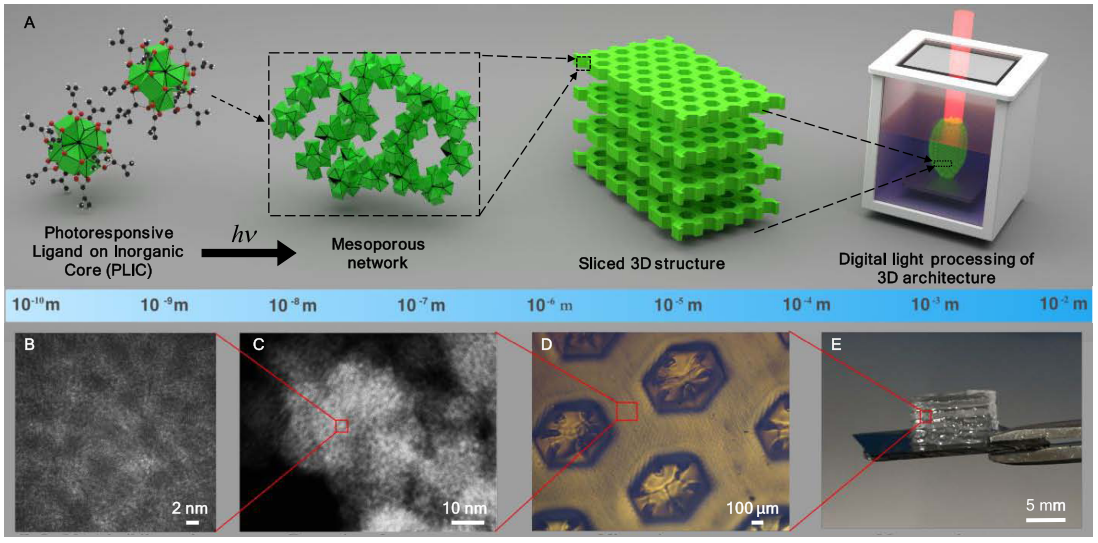

Figure 1. Three-dimensional printing photoresponsive ligand on inorganic core (PLIC) assembly. (A) Schematic representation of multilevel control in the printing process. PLIC materials are used as the building units and structured by a series of two-dimensional UV images in the 3D printer. (B) Building unit of zirconium oxide cluster with methacrylic acid (MAA) surface ligands. (C) Formation of pores via connecting the building units. (D) Example of the printed structure showing shape control for each layer. (E) Millimeter scale resulting parts with layer-by-layer stacking.

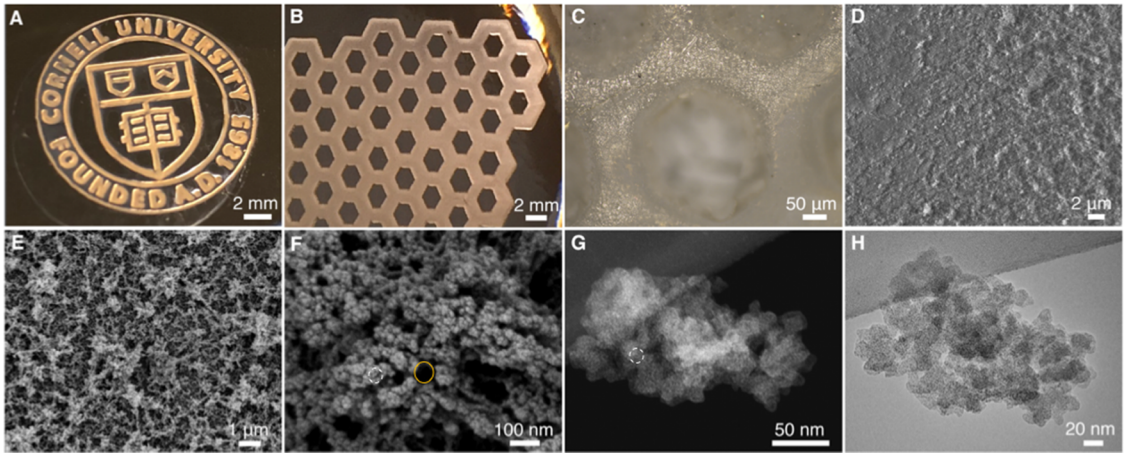

Figure 2. Hierarchical porous structures crossing 7 order magnitude in length scale. (A) Computer-aided design and printed Cornell logo. (B, C) Optical images of freestanding 3D objects. (D) Lower-magnification scanning electron microscopy (SEM) images showing a solid-like texture. (E, F) Higher magnification to show pores of the same sample as in (D). (G, H) scanning transmission electron microscopy (STEM and TEM) images showing the connection of building units to form a highly porous property. The circles by a dashed white line in (F) and (G) show the small mesopores; the circle by a solid orange line in (F) shows the large mesopores. (Logo used with permission. University logotype above is trademarked by Cornell University, Ithaca, New York.)

the nanoscale and the advantage of additive manufacturing at the macroscopic scale that enables conventional powder-like porous materials to be constructed to intricately designed architectures unattainable with conventional fabrication schemes. Integrating building blocks adopted from the colloidal nanocluster/nanoparticle community in 3D digital light processing presents an interesting interplay of the building block synthesis and externally triggered photopolymerization processing.

The fundamental building block of the PLIC 3D printing resin is based on $[Zr_6O_4(OH)_4]^{12+}$ with 12 methacrylic acid (MAA) ligands (Figure 1A). The structure extends from a prominent zirconium-based oxo cluster, which serves as building units to form micro- or mesoporous materials.[16,17] X-ray diffraction (XRD) patterns, Fourier transform infrared (FTIR) spectroscopy, nuclear magnetic resonance (NMR), and dynamic light scattering (DLS) confirm the match between synthesized and reported structures (Figures S1 and S4−S6).[16,17] The methacrylic acid ligands serve two functions: first to provide colloidal stability and second as a molecular connector by photopolymerizing the carbon double bond. As demonstrated below, we note that additional functionalities can be obtained by exchanging the surface-bound ligands after processing. The inherent compatibility with a broad spectrum of ligand chemistries makes this approach interesting for applications like separation that rely on programmable interactions between the fluid and the functionalized surface of the particle.

The connection between PLIC building blocks can be spatially programmed by controlling the region in which free-radical polymerization is photoinitiated (Figures 1C−E, S2, and S3). To fabricate the superstructure (the Cornell logo as

DOI: 10.1021/acs.chemmater.9b02761
Chem. Mater. 2019, 31, 10017−10022

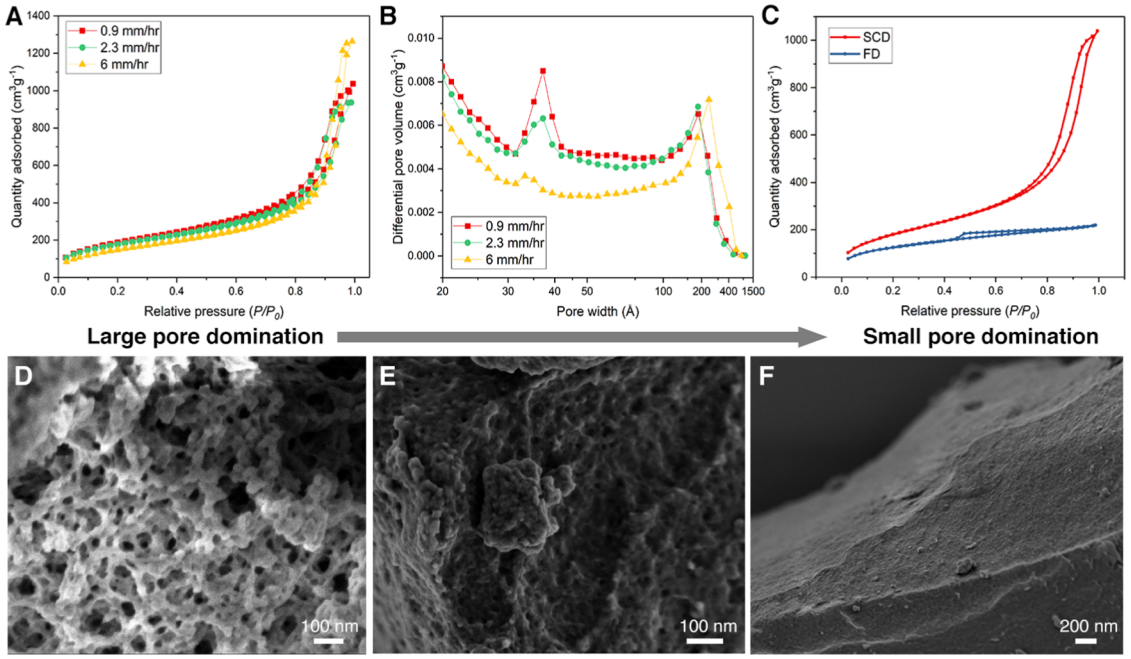

Figure 3. Print speed-controlled pore distribution. (A) Nitrogen sorption isotherms at 77 K with samples prepared in the print speed at 0.9, 2.3−6 mm/h. Slower print speed shows a higher BET surface area. (B) Pore distribution with different print speeds. The slower the print speed, the smaller the pore domination. (C) Effect of drying methods by comparing supercritical drying and freeze drying. (D−F) SEM images of different pore size dominations controlling by the print speed and drying method.

shown in Figure 2A,B), the PLIC ink was formulated by dissolving $Zr_6O_4(OH)_4$-MAA in the proper solvent with a UV free-radical photoinitiator (0.2 wt %) and used in the 3D printer. Fourier transform infrared spectroscopy of $Zr_6O_4(OH)_4$-MAA films before and after UV exposure in the 3D printer supports the interpretation that the C═C bonds cross-link the $Zr_6O_4(OH)_4$-MAA building blocks (see decreasing C═C vibrational signature near 1600 cm^{-1} after printing, Figure S4). Vis-à-vis 3D printing, this processing approach allows us to build the monolithic superstructure with the vertical speed of tens of millimeters per hour, which is only slightly slower than normal resin, showing both the potential to build devices and broader prospects for scalable nanofabrication (photopolymerization rates in Figure S8).

To gain deeper insights into the structure of the mesoporous films, we turned to scanning and transmission electron microscopies (SEM and TEM). Figure 2 demonstrates the breakdown of hierarchical length scales, supporting that primary, secondary, and tertiary networks can be constructed by 3D printing PLIC porous materials. At lower magnification, solid-like texture and different geometries show a precisely programmed fabrication without a clear defect over a large area (Figure 2A−D). At higher magnification, the SEM images reveal the spongy texture with small and large mesopores by connecting $Zr_6O_4(OH)_4$-MAA building blocks (Figure 2E−H). The netlike porous walls (Figure 2E) are constructed from closely packed building blocks (Figure 2F−H) resulting in a broad range of pore size distributions for large mesopores, which can be tailored by changing the printing conditions as we show below.

We confirmed the nanoscale porosity of 3D-printed structures by measuring nitrogen adsorption and desorption isotherms at 77 K. The profile shows the typical type IV isotherm with a hysteretic loop, indicating the feature of mesoporous materials. The printed superstructure exhibits high surface area, and the expected pore size distribution supported by the Brunauer−Emmett−Teller (BET) surface area with 679 m^2/g (Langmuir surface area: 1038 m^2/g) and the Barrett−Joyner−Halenda (BJH) theory calculation of 3.7 and 18 nm pore width dominations (Figure 3A,B) stands in good agreement with the electron microscopy results shown above.

The 3D-printed mesoporous structures reported in this work can be fabricated without the need for postprinting thermal annealing. In contrast to many of the recently reported 3D printing resins for glass, metals, and ceramic,[18−22] all of which require postprinting annealing, the mesoporous structures reported here can be formed in one step, which greatly simplifies the overall processing workflow. Successful implementation of PLIC inks requires the consideration of multiple interacting parameters including viscosity, solubility of the building blocks, light transmittance and radical stability, and solvent choice. We have investigated aliphatic and solvents (Figures S7 and S9) and found that using propylene glycol monomethyl ether acetate (PGMEA) as a solvent enables the formation of defect-free centimeter-scale glass-like honeycomb structures shown in Figure 2C. Benzene, on the other hand, appears to diminish the reactivity of the complexed radical causing the relative loose connection of building blocks,[23] which impacts both the porosity and the macroscopic appearance of the printed structure. In films processed from inks dissolved in benzene, the BET surface area decreases to 245 m^2/g, and the abundance of defects that turn transparent results to a white powder appearance can be observed (Figure S9).

The competing dynamics of building block self-assembly and externally triggered photopolymerization present an opportunity to control the mesoscale structure of the fabricated materials. Specifically, the extent to which clusters within the printed structure order depends on the time they have for self-

DOI: 10.1021/acs.chemmater.9b02761
Chem. Mater. 2019, 31, 10017−10022

assembly before externally triggered photopolymerization locks the building blocks in place. One result of this interplay is that the pore size distribution can be tuned by adjusting the 3D print speed. The trade-off between the print speed and the ratio of small and large mesopores is demonstrated with the BJH pore distribution in Figure 3A,B, from 0.9 to 6 mm/h. With higher print speed (i.e., less reaction time), the large 20 nm mesopores dominate and the signal for small mesopore is comparably negligible. By contrast, when the structures are printed at a slower speed (longer reaction time per layer), the porous structure is dominated by small mesopores 3.7 nm pores since the building blocks have more time to pack denser arrangements in each layer. The SEM images (Figure 3D–F) elucidate the diverse textures by tailoring the ratio of small and large mesopores, from periodically large pores to solid-like materials with small voids.

Removing the solvent without collapsing the internal pore structure presents a critical challenge in processing mesoporous materials.[24] In the case of the 3D-printed mesoporous structures at the focus of this paper, we found that freeze drying contributes to the shrinkage of the macroscopic structure due to the collapse of comparably fragile large pores. The loss in interparticle pores around 20 nm is evidenced with a narrow pore distribution at 3.7 nm and the lower BET surface area from 662 to 442 m^2/g (Figures 3C and S10). On the other hand, supercritical drying avoids the stresses arising due to capillary effects and helps to maintain the multilevel architecture.[25] By drying the printed structures in a supercritical CO_2 dryer, we can prevent the collapse of the pore structure and thereby form robust 3D-printed structures without compromising the high internal surface area. See the Supporting Information for the investigation of other parameters including thermal stability (Figure S12), resolution (Figure S13), control experiments of MAA (Figure S14), and the degree of photopolymerization (Figure S15).

To underscore the practical utility of the mesoporous structures that can be fabricated using the method introduced in this paper, we demonstrate the proof-of-concept 3D printing of a highly porous leaf. This choice of model structure was inspired by natural leaves, in which the hierarchical porous structure has been refined through billion years of evolution to endow all levels of hierarchy from macropores for fluid and nutrient transportation, micropores for gas diffusion, and nanopores for gas adsorption to perform complicated and optimal transport, and optical and chemical functionalities.[26,27] In light of the inherent multifunctionality enabled by the hierarchical porous superstructure of natural leaves, we 3D-printed a leaf as shown in Figure 4 (model shown in Figure S16). Although the 3D-printed leaf is still far from the complex multifunctional natural system that inspired it, this demonstration provides an important inspiration for emerging opportunities at the intersection of nanomaterials and 3D printing. We 3D-printed the designed leaf with macroscale veins like channels in the middle layer, microscale stomata like pores only on the back surface, and nanoscale spongy mesophyll cells like voids. Figure 4 indicates the printed features of both the structure and functions in the multilevel scale. The channels provide a similar function for mass transportation, and the stomata is for gas diffusion. Furthermore, we employed the thiol–ene chemistry to postfunctionalize the residual carbon double bond with cysteine ($C_3H_7NO_2S$), anchoring the amine group into the nanoscale pores.[28,29] To underscore the ability of the artificial

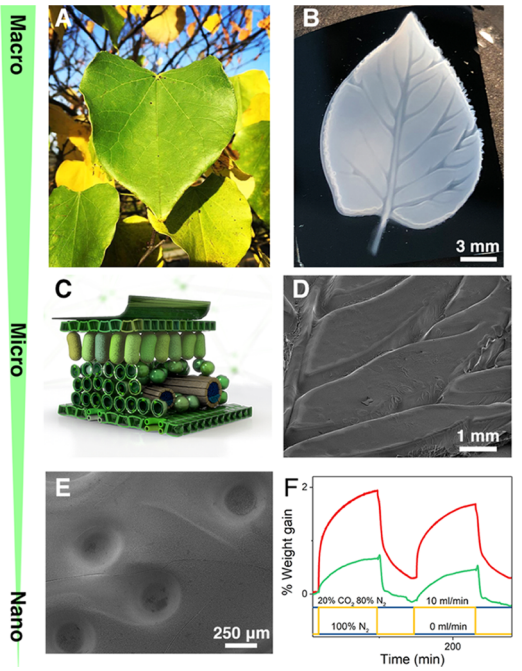

Figure 4. Complex devices like a leaf can be fabricated with 3D printing PLIC. (A) Photographic image of a leaf. (B) Photographic image of an artificial leaf. (C) Three-dimensional illustration of a leaf structure from a cross-sectional view. (D) SEM image of channels mimicking veins. (E) SEM image of small pores like stomata on the back surface. (F) CO_2 capturing capacity of 3D-printed artificial leaf. Red line: modified sample with amine group; green line: unmodified printed sample.

leaf to capture CO_2, we exposed the leaf to 20% carbon dioxide and 80% nitrogen under 30 °C and 1 atm. The nanoscale pores show the ability to adsorb up to 1.92 wt % carbon dioxide per gram of the leaf (nitrogen sorption result is discussed in Figure S11), approaching the 2.72 wt % capacity of similar Zr-based metal–organic framework.[30] Whereas the inorganic 3D-printed leaf does not, yet, include the complex multifunctionality found in natural leaves (fluid transport, photochemical reaction, etc.), this proof-of-concept structure nevertheless illustrates promising pathways to create programmable, 3D-printed functional porous materials.

In summary, we present a straightforward, cost-efficient, and fast route to fabricate hierarchical porous structures in a 3D printer. Preliminary studies present the possibility to harness both the nanoscale functionalities of porous materials and macroscale properties from the structure, certainly broadening the paradigm for original imaginations. Most important of all, the principle of PLIC design has the potential to be applicable to different cores and ligands, which we see as a promising bottom-up avenue for nanomaterial fabrication.

METHODS

Materials. All chemicals were purchased from Sigma-Aldrich. Nitrogen and carbon dioxide were purchased from Airgas. The Si substrate was purchased from University Wafer. All materials were used as received without any purification.

Synthesis of PLIC. $Zr_6O_4(OH)_4$-MAA precursors were synthesized by adopting the method as previously reported.[16,17,31,32] Briefly, Zr isopropoxide was dissolved in excess of methacrylic acids at 65 °C followed by the slow addition of a water/methacrylic acid mixture. It was left to react for 21 h, and the product was precipitated in water

DOI: 10.1021/acs.chemmater.9b02761
Chem. Mater. 2019, 31, 10017–10022

centrifuged at 8000 rpm. The final product was dried under vacuum overnight.

Additive Manufacturing. Ink for 3D printing was formulated by mixing dried PLIC nanoparticles from the last step, photoinitiator and solvent. For example, 150 mg of synthesized $Zr_6O_4(OH)_4$-MAA and 1 mg of photoinitiator, diphenyl(2,4,6-trimethylbenzoyl) phosphine oxide, were added into 1 mL of PGMEA. Inks were purged with nitrogen flow for 10 min before usage. Samples are printed with the homemade top-down digital light processing (DLP) 3D printer with a 385 nm wavelength and intensity around 10 mW/cm^2. The general workflow involves slicing the desired 3D architecture into a series of images, which are then exposed as a sequence of UV patterns to define the cross section for each additive layer.

Activation and Functionalization. All printed samples were washed with toluene. For supercritical carbon dioxide drying, samples were exchanged with methanol for 48 h with renewing the solvent for every 12 h and then dried in a Leica CPD300 critical point dryer. As for freeze drying, samples were immersed in cyclohexane for 48 h with renewing the solvent for every 12 h. After frozen at −20 °C with three freeze−thaw cycles, the samples were dried with a freeze dryer for 12 h.

For amine-functionalized samples, the dried samples were immersed in 3 mL methanol with 90 mg of cysteine for 1 day and then exposed to a 254 nm UV light for 5 min. Samples were washed with methanol for several times and directly dried in the hood.

General Characterization Methods. Powder X-ray diffraction characterization was carried out on a Bruker-AXS D8 Discover diffractometer using a Cu Kα radiation at λ = 1.54 Å by depositing the powder on a glass substrate. The FTIR was conducted on a Bruker Hyperion FTIR spectrometer and microscope. A background scan was collected before each measurement (64 scans); the sample scan was an average of 64 scans, and the resolution was set to 4 with a data spacing of 0.482 cm^{-1}. Thermogravimetric analysis (TGA) was performed on a TGA Q500 (TA Instruments Inc.). The CO_2 capturing property of the artificial leaf was calculated based on the weight gain during the adsorption. Dynamic light scattering (DLS) (Zetasizer Nano 90; Malvern, Worcestershire, U.K.) was used to measure the hydrodynamic diameter of NPs dispersed in the solvent. The photorheometer test was done on DHR3, TA instruments with the light source Omnicure Series 1500. Parallel plate geometry with a gap of 750 μm and the 365 nm filter with the controlled power being 10 mW/cm^2 were used. ^{1}H NMR spectra were recorded on a Bruker AV500 spectrometer with 16 scans and a 45° excitation pulse. NMR data was analyzed by MestReNova. Photodifferential scanning calorimetry measurements were conducted on a TA Instrument Q1000 with the same light source used in photorheometer. Measurements were tested with an equilibrium temperature at 30 °C, and a 50 mL/min nitrogen gas was passed through during all the experiments.

Electron Microscope Characterization. SEM images were acquired using a Zeiss Gemini 500 SEM and Tescan Mira3 FESEM. STEM and TEM images were taken using an FEI Tecnai F20 S/TEM. Printed samples were ground to powders and tapped by the wafer or TEM grid for the imaging. PLIC nanoparticles were dissolved in toluene in the concentration of 5 mg/mL and then drop-coated onto the TEM grid. Figure 3D,E shows the samples in Figure 3A, 6 and 0.9 mm/h, respectively, with supercritical drying, and F is the sample in Figure 3C with freeze drying. Artificial leaf was processed with the gold sputtering before imaging.

Nitrogen Adsorption Measurements. Nitrogen sorption isotherms were measured at 77 K on a Micromeritics ASAP 2460. Normally, tens of milligrams of printed samples were transferred into preweighed tubes. As for $Zr_6O_4(OH)_4$-MAA crystal, 100 mg of the material was added. All of the samples were degassed under vacuum in room temperature for 2 h before the test. The specific surface area and pore diameter were calculated using the Brumauer−Emmett−Teller (BET) and Barrett−Joyner−Halanda (BJH) method, respectively.

■ ASSOCIATED CONTENT

Supporting Information

The Supporting Information is available free of charge on the ACS Publications website at DOI: 10.1021/acs.chemmater.9b02761.

Nanoparticle-related inks for additive manufacturing, building block characterization (XRD, TEM, FTIR, NMR, and DLS), mechanism discussion, solvent comparison, study of print speed, more BET and consistency results, thermal stability, resolution, and degree of photopolymerization (PDF)

■ AUTHOR INFORMATION

Corresponding Author

*E-mail: th358@cornell.edu.

ORCID

Jen-Yu Huang: 0000-0003-1906-7857
Hong Xu: 0000-0001-7918-1454
Christopher K. Ober: 0000-0002-3805-3314
Tobias Hanrath: 0000-0001-5782-4666

Notes

The authors declare no competing financial interest.

■ ACKNOWLEDGMENTS

J.-Y.H. and T.H. acknowledge support from NSF-CMMI 1635433. This work made use of the Cornell Center for Materials Research Shared Facilities, which are supported through the NSF MRSEC program (DMR-1719875). This work was performed, in part, at the Cornell NanoScale Facility, a member of the National Nanotechnology Coordinated Infrastructure (NNCI), which is supported by the National Science Foundation (Grant ECCS-1542081). The authors thank Sophie Ifan Wu for providing leaf photograph.

■ REFERENCES

(1) Shtein, Z.; Shoseyov, O. When bottom-up meets top-down. *Proc. Natl. Acad. Sci. U.S.A.* **2017**, *114*, 428−429.

(2) Li, P.; et al. Bottom-up construction of a superstructure in a porous uranium-organic crystal. *Science* **2017**, *356*, 624−627.

(3) Allendorf, M. D.; Stavila, V. Crystal engineering, structure-function relationships, and the future of metal-organic frameworks. *CrystEngComm* **2015**, *17*, 229−246.

(4) Slater, A. G.; Cooper, A. I. Function-led design of new porous materials. *Science* **2015**, *348*, aaa8075.

(5) Zheng, X.; et al. Multiscale metallic metamaterials. *Nat. Mater.* **2016**, *15*, 1100−1106.

(6) Whitham, K.; et al. Charge transport and localization in atomically coherent quantum dot solids. *Nat. Mater.* **2016**, *15*, 557−563.

(7) Yang, X.-Y.; et al. Hierarchically porous materials: synthesis strategies and structure design. *Chem. Soc. Rev.* **2017**, *46*, 481−558.

(8) Furukawa, S.; Reboul, J.; Diring, S.; Sumida, K.; Kitagawa, S. Structuring of metal−organic frameworks at the mesoscopic/macroscopic scale. *Chem. Soc. Rev.* **2014**, *43*, 5700−5734.

(9) Seoane, B.; Castellanos, S.; Dikhtiarenko, A.; Kapteijn, F.; Gascon, J. Multi-scale crystal engineering of metal organic frameworks. *Coord. Chem. Rev.* **2016**, *307*, 147−187.

(10) Korstanje, T. J.; Ivar van der Vlugt, J.; Elsevier, C. J.; de Bruin, B. Hydrogenation of carboxylic acids with a homogeneous cobalt catalyst. *Science* **2015**, *350*, 298−302.

(11) Truby, R. L.; Lewis, J. A. Printing soft matter in three dimensions. *Nature* **2016**, *540*, 371−378.

DOI: 10.1021/acs.chemmater.9b02761
Chem. Mater. 2019, 31, 10017−10022

(12) Yang, Y.; et al. Biomimetic Anisotropic Reinforcement Architectures by Electrically Assisted Nanocomposite 3D Printing. *Adv. Mater.* **2017**, *29*, No. 1605750.
(13) Lacey, S. D.; et al. Extrusion-Based 3D Printing of Hierarchically Porous Advanced Battery Electrodes. *Adv. Mater.* **2018**, *30*, No. 1705651.
(14) Tumbleston, J. R.; Shirvanyants, D.; et al. Continuous liquid interface production of 3D objects. *Science* **2015**, *347*, 1349−1352.
(15) MacDonald, E.; Wicker, R. Multiprocess 3D printing for increasing component functionality. *Science* **2016**, *353*, No. aaf2093.
(16) Schubert, U. Cluster-based inorganic−organic hybrid materials. *Chem. Soc. Rev.* **2011**, *40*, 575−582.
(17) Užarević, K.; et al. Mechanochemical and solvent-free assembly of zirconium-based metal−organic frameworks. *Chem. Commun.* **2016**, *52*, 2133−2136.
(18) Eckel, Z. C.; et al. Additive manufacturing of polymer-derived ceramics. *Science* **2016**, *351*, 58−62.
(19) Kotz, F.; et al. Three-dimensional printing of transparent fused silica glass. *Nature* **2017**, *544*, 337−339.
(20) Vyatskikh, A.; et al. Additive manufacturing of 3D nano-architected metals. *Nat. Commun.* **2018**, *9*, No. 593.
(21) Zanchetta, E.; et al. Stereolithography of SiOC Ceramic Microcomponents. *Adv. Mater.* **2016**, *28*, 370−376.
(22) Schmidt, J.; Elsayed, H.; Bernardo, E.; Colombo, P. Digital light processing of wollastonite-diopside glass-ceramic complex structures. *J. Eur. Ceram. Soc.* **2018**, *38*, 4580−4584.
(23) Ito, O.; Matsuda, M. Solvent effect on rates of free-radical reactions. 2. Addition of the p-(dimethylamino)benzenethiyl radical to.alpha.-methylstyrene. *J. Phys. Chem. A* **1984**, *88*, 1002−1005.
(24) Farha, O. K.; Hupp, J. T. Rational Design, Synthesis, Purification, and Activation of Metal−Organic Framework Materials. *Acc. Chem. Res.* **2010**, *43*, 1166−1175.
(25) Nelson, A. P.; Farha, O. K.; Mulfort, K. L.; Hupp, J. T. Supercritical Processing as a Route to High Internal Surface Areas and Permanent Microporosity in Metal−Organic Framework Materials. *J. Am. Chem. Soc.* **2009**, *131*, 458−460.
(26) Zheng, X.; et al. Bio-inspired Murray materials for mass transfer and activity. *Nat. Commun.* **2017**, *8*, No. 14921.
(27) Zhou, H.; et al. Leaf-architectured 3D Hierarchical Artificial Photosynthetic System of Perovskite Titanates Towards CO_2 Photoreduction Into Hydrocarbon Fuels. *Sci. Rep.* **2013**, *3*, No. 1667.
(28) Xu, H.; Gao, J.; Jiang, D. Stable, crystalline, porous, covalent organic frameworks as a platform for chiral organocatalysts. *Nat. Chem.* **2015**, *7*, 905−912.
(29) Yang, S.; et al. Selectivity and direct visualization of carbon dioxide and sulfur dioxide in a decorated porous host. *Nat. Chem.* **2012**, *4*, 887−894.
(30) Hu, Z.; Wang, Y.; Shah, B. B.; Zhao, D. CO_2 Capture in Metal-Organic Framework Adsorbents: an Engineering Perspective. *Adv. Sustainable Syst.* **2019**, *3*, No. 1800080.
(31) Kosma, V.; Kasahara, K.; Xu, H.; Odent, J.; Ober, C. K. Elucidating the patterning mechanism of zirconium-based hybrid photoresists. *J. Micro/Nanolithogr., MEMS, MOEMS* **2017**, *16*, No. 041007.
(32) Kickelbick, G.; Schubert, U. Oxozirconium Methacrylate Clusters: $Zr_6(OH)_4O_4(OMc)_{12}$ and $Zr_4O_2(OMc)_{12}$ (OMc = Methacrylate). *Chem. Ber.* **1997**, *130*, 473−478.

DOI: 10.1021/acs.chemmater.9b02761
Chem. Mater. 2019, 31, 10017−10022